www.acsnano.org

Lasing from Brillouin Zone Folding Guided Resonances

Matthew R. Chua, Lu Ding,* Xiao Liang, Corentin Dabard, Wudeng Wang, Syed Akhil, Emek Goksu Durmusoglu, Febiana Tjiptoharsono, Hilmi Volkan Demir,* Ramón Paniagua-Domínguez, and Arseniy I. Kuznetsov*



Downloaded via BILKENT UNIV on October 9, 2025 at 14:00:27 (UTC). See https://pubs.acs.org/sharingguidelines for options on how to legitimately share published articles.

Cite This: ACS Nano 2025, 19, 34677-34685



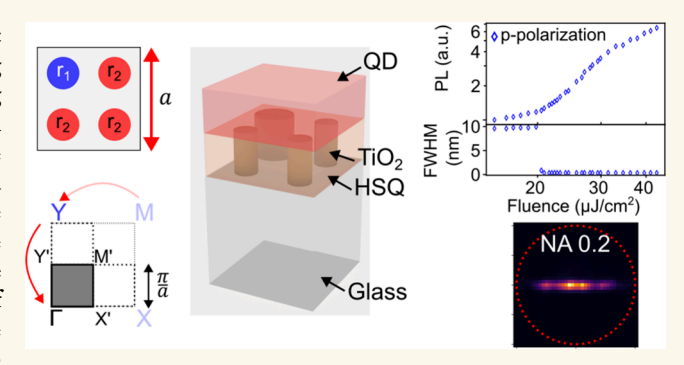
ACCESS

Metrics & More

Article Recommendations

s Supporting Information

ABSTRACT: High-quality factor (Q-factor) nanophotonic cavities are critical components in applications such as lasing and nonlinear optics. However, to obtain out-of-plane lasing emission and a low lasing threshold, the lasing mode must fulfill the contradictory requirement of coupling to the light cone while maintaining a high Q-factor. One relatively unexplored method to design such modes consists of using a Brillouin Zone folding guided resonance (BZF-GR) as the high Q-factor mode for lasing. In such a design, guided modes are "folded" into the light cone via periodic perturbations, allowing fine control of the Q-factor throughout momentum space. In this paper, we experimentally demonstrate the use of such a BZF-GR to



achieve vertical emission lasing from a nanophotonic cavity with colloidal quantum dots as a gain medium. The lowest lasing threshold fluence under nanosecond pump is $(20.4 \pm 0.3) \mu \text{J cm}^{-2}$. When considering the absorption, this value falls to (4.08) \pm 0.08) μ J cm⁻². This work presents a method of designing lasing modes that may be further developed for use in lowthreshold nanoscale lasers.

KEYWORDS: vertical lasing, two-dimensional metasurfaces, Brillouin zone folding, quantum dots, nanosecond lasing

INTRODUCTION

Lasers incorporating solution-processed gain media have garnered intense attention due to their apparent ease of fabrication, and great progress in lowering the lasing threshold with improvements from both material and cavity design concepts. 1-6 One convenient approach is to use a "lateral" cavity, where optical feedback is in the substrate plane, usually based on guided modes. Such designs often involve subwavelength patterned periodic structures, which can be broadly classified as metasurfaces, to engineer the lateral mode coupling. This allows the laser to be fabricated by depositing a modest thickness of gain material on a prepatterned periodic structure to form the whole cavity, 1-8 which is particularly amenable to integration with solution-processed emitters.

A low lasing threshold is critical when sensitive emitters such as quantum dots (QDs) are used as the gain medium as they tend to degrade more easily, and may be damaged, especially by thermal effects, by optical excitation before the lasing regime is reached. 1,2 From the materials angle, it is then critical to lower the excitation threshold by increasing the intrinsic gain and/or decreasing the gain threshold. In II-VI nanocrystals, advances in synthesis has led to a variety of size,

composition and shape control methods, allowing engineering of the electronic structure, recombination rates, and gain thresholds leading to the landmark demonstrations of continuous wave optically pumped lasing by Fan et al. (8 kW cm⁻² threshold at −20 °C) and electrically pumped amplified spontaneous emission (ASE) by Ahn et al. 1,2,8-16 Other notable solution-processed materials such as lead halide perovskites have also seen substantial advances, with demonstrations of continuous wave optically pumped lasing, and polariton emission at room temperature in Fabry-Perot and distributed feedback structures. 3,17-23

From the photonic point of view, a low lasing threshold requires a high Q-factor lasing cavity mode as it exhibits low radiative losses and a long photon lifetime, which aids the generation of optical gain and eventually lasing in the

Received: May 21, 2025 Revised: September 11, 2025

Accepted: September 12, 2025 Published: September 25, 2025





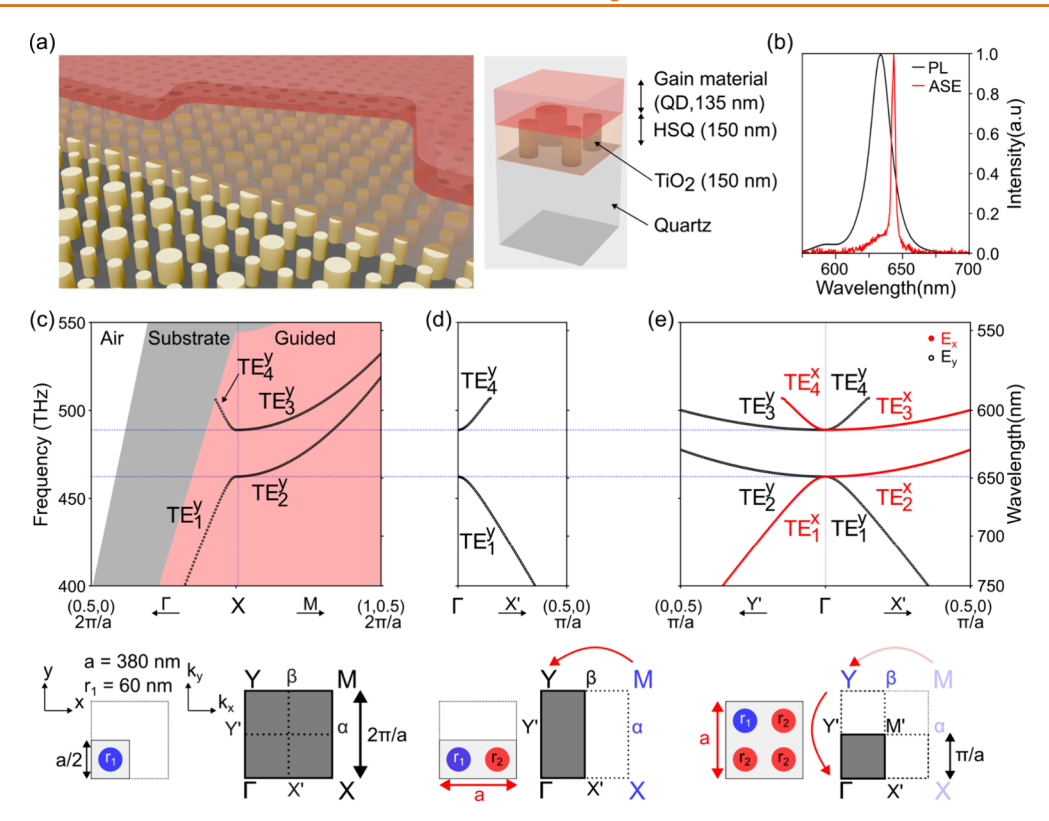


Figure 1. Brillouin zone folding lasing cavity design concept. (a) (Left) A schematic of the lasing device composed by a QD thin film on a TiO₂ nanoantenna array planarized by HSQ on a quartz substrate. (Right) A cross-section view of the unit cell which contains $4x \text{ TiO}_2$ cylinders of 150 nm height and a QD film of 135 nm. (b) Normalized emission spectra of the QD gain medium under weak excitation PL and ASE conditions with nanosecond stripe pump. (c-e) Evolution of the calculated transverse electric (TE) band structure based on BZF from 1×1 single-cylinder cell to a 2×2 supercell when r_1 and r_2 are considered to have an infinitesimal perturbation. (c) TE^y modes along $\Gamma \to X \to M$ near X of a 1×1 single-cylinder cell. For clarity only the lowest TE guided modes are shown. (d) Modes of a 2×1 supercell, with $P_x = 2P_y = a$, along $\Gamma \to X$, modes TE^y_{1,4} are translated from X to Γ . (e) Modes of the 2×2 supercell along $Y' \to \Gamma \to X'$. Along $X \to X'$, two additional folded modes with E_x polarization appear. Along $Y \to Y'$ the mode structure is identical but with orthogonal polarizations. The blue line at the TE band gap serves as a guide to the eye.

system.^{24,25} However, to obtain out-of-plane emission, it is also necessary for the mode to have a finite coupling to the light cone, which reduces the *Q*-factor. These opposing factors necessitate fine control of the mode radiation constant to balance external coupling, while maintaining an acceptably high mode *Q*-factor, and apply to all forms of outcoupling engineering, not just vertical emission.^{26–28}

A popular pathway to design surface-emitting metasurface laser modes typically uses Bound States in the Continuum (BIC) as a design template. 29,30 At the BIC point, external radiation is suppressed by cancellation of multiple radiative channels through destructive interference, leading to a theoretically infinite Q-factor.³¹ An isolated BIC at k_{BIC} i.e., one with no other BICs nearby in parameter space, typically has a Q-factor falloff as the in-plane wavevector (k) deviates from the BIC of the form $Q \propto \frac{1}{|\mathbf{k} - \mathbf{k}_{BIC}|^2}$. 32,33 Coupling to the light cone is expected to be from the quasi-BIC states in the vicinity of the BIC with a lower Q, as the BIC point itself cannot couple to the far field. This leads to a "donut" or "lobed" radiation pattern typically observed in lasing from BICs, which might be undesirable for directed emission applications such as imaging or communication.^{34–36} In a realistic device, there are additional complications. First, in finite-size metasurfaces, the accessible momentum states are discretized, typically leading to a lower accessible Q-factor than at the precise BIC point. 37,38 Second, fabrication limitations

introduce disorder, which couples the target mode with other lossy channels, also lowering the effective *Q*-factor. To counter these effects, merging or "super"-BIC designs have been proposed and demonstrated. The idea of such designs is to position several BICs in the vicinity of a desired k-space point to reduce the often quoted $Q \propto 1/|\mathbf{k}|^2$ falloff and scattering losses. This can be done by splitting a high topological charge BIC into separate BICs, or by tuning separate BICs together. ^{25,32,33,40}

In this paper, we instead apply Brillouin zone folding (BZF), a conceptually different method to generate high Q-factor states in the light cone. One way to describe the BZF design is as follows: an elementary unit cell with periodicity (P_0) is first defined to generate guided modes that are not coupled to the light cone, and consequently, have theoretically infinite Qfactor. A weak, controlled, periodic perturbation with a period of $P_1 > P_0$ can be applied to extend the real space period to P_1 and reduce the BZ size. In the perturbative limit, this remaps the modes of the original structure into the new "folded" BZ, and modes now coupled to the light cone by this P_1 perturbation largely retain their original characteristics, especially their high Q-factor. ^{27,28,41,42} The symmetry of the resulting supercell of period P_1 determines which (if any) modes become symmetry-protected BZF-BICs or leaky guided resonances (BZF-GRs) at high symmetry points.⁴³ BZF-BICs are essentially symmetry-protected BICs, but with a reduced Q-factor falloff $(Q \propto 1/\alpha^2 |\mathbf{k}|^2$, where α is a geometric

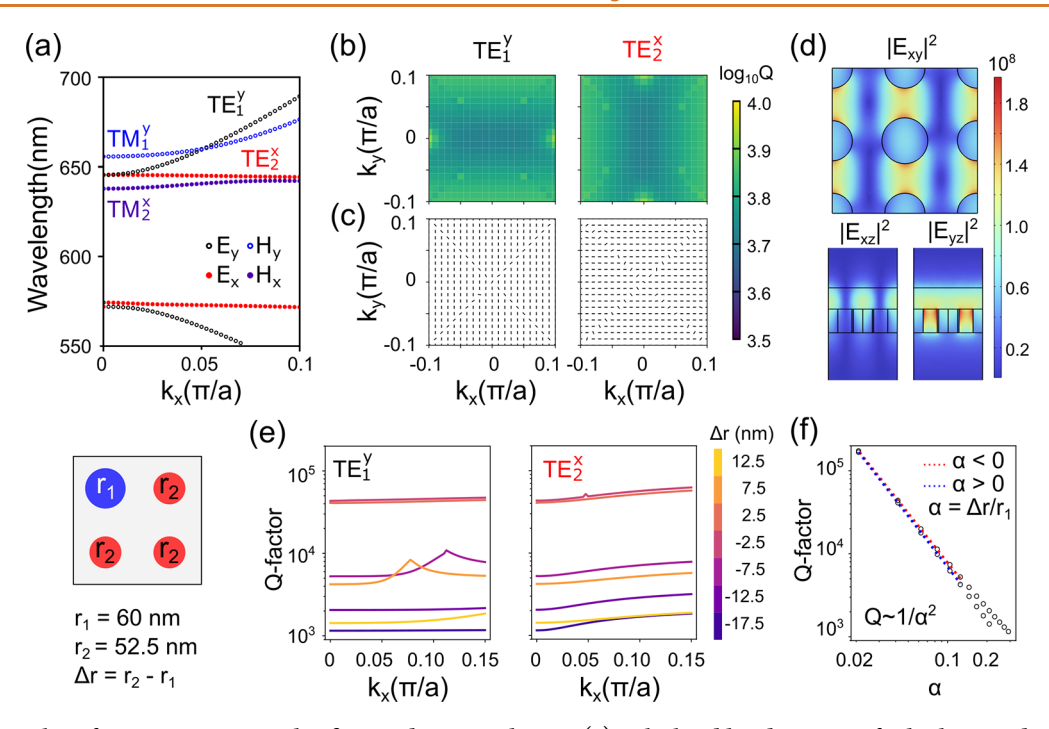


Figure 2. Mode analysis for BZF structure with a finite radius perturbation. (a) Calculated band structure for both TE and TM modes of a 2 \times 2 supercell with $(r_1, \Delta r) = (60, -7.5)$ nm along $\Gamma \to X'$. (b) 2D k-space maps of the Q-factor and (c) far-field polarization maps of the near Γ point of TE₁ (left) and TE₂ (right) for $(r_1, \Delta r) = (60, -7.5)$ nm. (d) Corresponding mode profile $|E|^2$ of TE₁ mode at Γ point along xy (middle height of TiO₂ cylinders), xz and yz planes. (e) Simulated Q-factor of TE₁ and TE₂ modes with $r_1 = 60$ nm and Δr varying from -17.5 to 12.5 nm along k_x . (f) Q-factor at the Γ point scales with the asymmetry factor $(\alpha = \Delta r/r_1)$ showing the $Q \propto 1/\alpha^2$ dependence. The Q-factor dependence differs slightly with the sign of α , likely due to the simplified definition of α .

asymmetry factor) from the BIC point. On the other hand, BZF-GRs have a broadband, relatively flat *Q*-factor $(Q \propto 1/\alpha^2)$ with no symmetry forbidden radiation. ^{28,41}

The high Q-factor attainable by this BZF design has been experimentally demonstrated by several authors. For example, Wang et al. used a 1D (C_2 symmetry-breaking perturbation) design of air holes in silicon. 41 Huang et al. also discussed the generality of a weak perturbation approach, and demonstrated a high-Q-factor silicon-on-insulator metasurface using a patterned photoresist layer on silicon, which was also demonstrated by Fang et al.^{27,44} In plasmonic systems, de Gaay Fortman et al. have also recently demonstrated high-Qfactor BZF modes with a silver nanoparticle array. 45 BZF modes may additionally be more robust to disorder than conventional BIC modes, making this design more amenable to large-scale fabrication and process integration.⁴¹ Here, we focus on engineering the fundamental transverse electric (TE) BZF-GR mode in a two-dimensional (2D) metasurface to obtain vertical emission lasing with an optically pumped colloidal QD gain medium. Our lowest obtained threshold fluence with 532 nm nanosecond pump is (20.4 \pm 0.4) μJ cm⁻² per pulse, which corresponds to $(4.08 \pm 0.08) \mu \text{J cm}^{-1}$ when considering the absorption of the material at the pump wavelength, which compares favorably with other metasurface laser designs using similar emitters. 46,8,47,48

RESULTS

Concept and Design. The lasing cavity consists of a ${\rm TiO_2}$ cylinder metasurface planarized by cured hydrogen silsesquioxane resist (HSQ) with a film of QDs deposited on top. A quartz substrate is used with the top cladding being air. A cutaway section of an array and the corresponding periodic

supercell are schematically illustrated in Figure 1a. The supercell is square and consists of 4 TiO2 cylinders, arranged in a square array equidistant from each nearest neighbor with the radius of one cylinder (r_1) different from the other three (r_2) . For fixed layer thicknesses (e.g., TiO₂ = 150 nm, QD = 135 nm), tuning the radii of the TiO₂ cylinders allows the GR modes to be tuned to match the QD gain spectrum, which can be approximated by the ASE spectrum (Figure 1b). The gain medium is a solution-processed film of compact continuousgrade QDs (CdSe/Cd_xZn_{1-x}Se/ZnSe_{0.5}S_{0.5}/ZnS). The QDs are synthesized with built-in strain, a structure which can reduce the material gain threshold by splitting the band edge degeneracy while keeping a low Auger recombination rate. ^{13,46,49} By finely tuning the thicknesses of successive shells, small and highly monodisperse QDs with narrow photoluminescence (PL) of ~19 nm full width at halfmaximum (FWHM) in solid thin film are synthesized. The deposited QD films exhibit low roughness, allowing for reduced scattering losses in the metasurface modes. Under a 532 nm nanosecond stripe pump, the film exhibits an ASE spectrum concentrated around the biexciton emission (<5 nm FWHM at \sim 643 nm) with a threshold of \sim 150 μ J cm⁻² and an estimated modal gain coefficient of 90 \pm 10 cm⁻¹. For enhanced stability, the solution-processed films are prepared and encapsulated in a nitrogen atmosphere. Further details on the synthesis and characterization of the QDs and on the gain material characterization are contained in the experimental methods (in Supporting Information Sections 1 and 2, respectively).

Our mode is designed by targeting the X point mode in the unperturbed lattice, which is then moved to the Γ point by period doubling. From the BZF perspective, the final band structure may be considered to evolve from that of a 1 \times 1

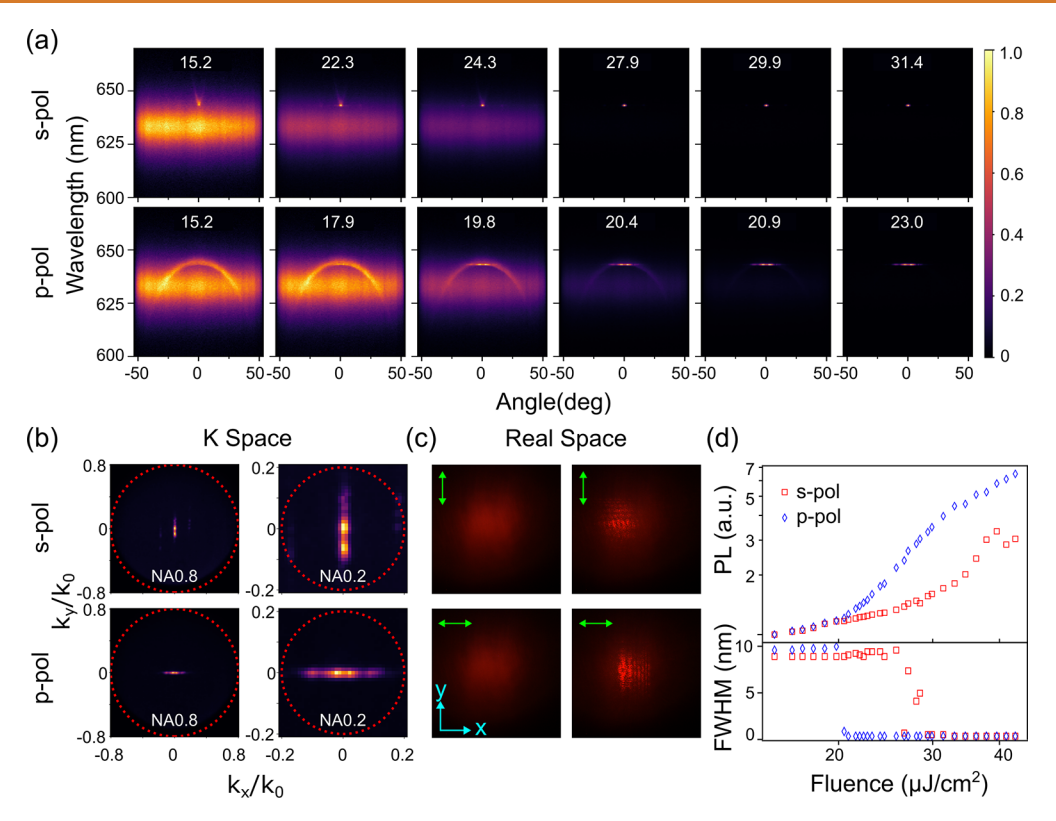


Figure 3. Lasing characteristics of the BZF-GR mode for the lowest threshold array $(r_1, \Delta r) = (60, -2.5)$ nm. (a) Power dependent normalized PL spectra for s- and p-polarized emissions. Numbers in each graph indicate the incident pumping pulse energy on the sample in nJ unit. (b) Back focal plane images for s- and p-polarized emission above the lasing threshold $(\sim 40 \,\mu\text{J cm}^{-2})$ at NA values of 0.8 and 0.2 (c) Optical images of the array at low (left) and high (right) pumping pulse energies under different polarizer alignments. The polarizer alignment, along with the polarization labeling is in the bottom left of each image. (d) Integrated PL emission (top) and FWHM (bottom) plotted against the pump fluence.

single-cylinder cell to a 2×2 supercell through sequential "folding" operations, for instance, where the original BZ is folded once along the x and then y direction. Here, we limit our discussion of the band folding to the TE modes for clarity (Figure 1c-e). As an example, we consider the single-cylinder cell of a/2 = 190 nm in period and a cylinder radius $r_1 = 60$ nm. Figure 1c shows the calculated TE modes (black circles) along the $\Gamma \to X \to M$ direction of the original BZ near the X point. The fundamental modes near the X point are guided modes and are E_{ν} polarized. The modes are thus labeled TE_{i}^{ν} from lowest to highest frequency, with the target mode being TE₁ and TE₂. Due to symmetry, an identical band structure exists near the Y point (along the $\Gamma \to Y \to M$ direction) but with E_x polarized modes. Introducing an infinitesimal perturbation on the radius of every other cylinder along the x-direction, the unit cell is now a 1 \times 2 bicylinder cell (1 r_1 , $1r_2$). P_x is doubled, so the BZ folds in half along k_x with X \rightarrow M folding onto $\Gamma \to Y$. The $X \to X'$ branch is therefore folded to $\Gamma \to X'$ (Figure 1d). Expanding from a 1 × 2 to a 2 × 2 supercell $(1r_1, 3r_2)$, P_v is doubled, resulting in a k_v -directed folding $Y \to \beta$ onto $\Gamma \to X'$. As a result, along $\Gamma \to X'$, we observe not only the $TE_{1.4}^y$ modes but also the $TE_{2.3}^x$ modes that originate from $Y \rightarrow \beta$ in the unfolded dispersion (Figure 1e, right panel). Symmetrically, a similar situation happens along $\Gamma \to Y'$ (Figure 1e, left panel). It should be noted that although all these modes are TE polarized based on their internal field, in measurements in which a linear polarizer is used, half of the modes will appear in the s- or p-polarizations. For instance, if s- and p-polarizations are defined with the

polarizer aligned to the x- or y-direction, respectively, TE^x modes will appear s-polarized, and TE^y modes will appear p-polarized.

Given a finite-size perturbation $\Delta r = r_2 - r_1$, these BZF modes will undergo further interaction, which adjusts their mode profile and wavelength. As the Q-factor of the modes is related to the size perturbation, we index the various design combinations of cylinder radii as $(r_1, \Delta r)$ nm. Figure 2a shows the band structure near the Γ point of $(r_1, \Delta r) = (60, -7.5)$ nm along $\Gamma \to X'$. The transverse magnetic (TM) H_v and H_x polarized modes TM_{1,2} are generally present near the TE modes as well, originating from the same folding as described for TE modes. With this design, the TE₁ and TE₂ bands along $\Gamma \to X'$ will become BZF-GRs and are degenerate at the Γ point, while the TM modes will form nondegenerate BZF-BICs. The second lowest group BZF modes (TE_3^x, TE_4^y) are separated by the original photonic bandgap, sufficiently far from the QD emission spectrum, and any originally present unfolded modes are at yet shorter wavelengths. The characteristics of the TE modes are further studied to confirm their character. Figure 2b shows the Q-factor, and Figure 2c shows the far-field polarization in 2D momentum space around the Γ point for TE_1^y (left) and TE_2^x (right). As expected for a GR, the Q-factor is relatively constant, while the far field is linearly polarized according to the modal field polarization. In Figure 2d, the mode intensity profile for TE₁ confirms the TE character with a spatial mode-gain overlap of approximately 40%. For $r_1 = 60$ nm with varying Δr , we see that the GR mode Q-factor retains similar characteristics (Figure 2e) with a

relatively flat Q-factor, apart from some local modulation at finite k_x likely due to mode crossings. Extracting the Q-factor for TE_1^y , at the Γ point, we find that the Q-factor approximately scales as $Q \propto \alpha^{-2}$ where $\alpha = \Delta r/r_1$. There is a slight variation in the dependence on the sign of α , which is likely due to our simplified definition of α . Similar characterization for the other modes is appended in Figures S5 and S6. Overall, the BZF-GR can sustain a high Q-factor with a controllably small Δr perturbation. The spatial mode overlap is \sim 40%, and it should be possible to obtain low-threshold vertical emission lasing from the TE BZF-GR.

EXPERIMENTAL RESULTS AND DISCUSSION

A series of cavities is fabricated with period a = 380 nm and varying $(r_1, \Delta r)$ combinations to target the TE₁ modes in the QD gain spectrum. Details of the nanofabrication are appended in the methods and Figure S6. The low fluence angle-resolved PL verifies the general accuracy of the fabrication (Figure S7). The lowest lasing threshold is observed in an array (60, -2.5) nm, which is the nominal minimum asymmetry prepared in nanofabrication, and the results are presented in Figure 3. In Figure 3a, the angle-resolved PL spectra for s- and ppolarizations are shown at representative pump energies. At low pumping pulse energies, the TE GR modes have a low contrast with the PL background since at low Δr the Q-factor is high. As the TE GRs are linearly polarized and based on our collection geometry, TE₁ appears in the s-polarization (E_{ν}) , while TE_2^x appears in the ppolarization (E_x) . The TM modes are visible only at relatively high values of Δr and couple weakly to the PL, likely due to the lower spatial mode overlap (Figure S8). As pump power increases, the mode visibility increases significantly until only a small section around k = 0and at ~643 nm is visible. The lasing emission forms a linearly polarized bar in k-space (Figure 3b) for both s- and p-polarization; this is likely due to the relatively constant Q-factor across the GR branch. There is some modulation in the intensity across the emission beam, possibly due to coupling to the finite size of the array, or other local modulation that competes with the low Δr perturbation. In the real space optical images, at low power, there is no obvious mode coupling, while at higher power, interference fringes are apparent in the emission from the array (Figure 3c).

Extracting the light in–light out (L-L) curves and full widths at half-maximum (FWHM) of the emission from the PL spectrum, we obtain Figure 3d. Lasing is confirmed by the s-shaped curve in the L-L plot, where the nonlinear increase in PL intensity is concurrent with an abrupt decrease of the FWHM from $\sim\!9$ to $\sim\!0.4$ nm (limited by the spectrograph system). However, we can see that the thresholds in both polarizations are distinct, at $(20.4\pm0.4)~\mu\mathrm{J~cm^{-2}}$ in the p-polarization and at $(27.9\pm1.4)~\mu\mathrm{J~cm^{-2}}$ in the s-polarization, based on the FWHM reducing to 50% of the initial value. A rough estimate of absorption of the array at the pump wavelength of 532 nm is 20% (Figures S9 and S10), giving an effective lasing threshold as low as $(4.08\pm0.08)~\mu\mathrm{J~cm^{-2}}$.

Many fabricated arrays (20) with varying $(r_1, \Delta r)$ also exhibit lasing behavior and we further investigate their properties (Figure 4). The L-L curves and line widths are extracted as described earlier, and the lasing threshold (E_{th}) is determined (Figures S11–S16). Motivated by the differing thresholds for s- and p-polarizations for (60, -2.5) nm, we characterize the lasing behavior of two groups of arrays ($r_1 = 50$, 60 nm) at two different orientations (0°, 90°, Figure 4a-d). Generally, the thresholds in s- and p-polarizations are not the same, and when lasing is observed in both polarizations at distinct thresholds, the relative threshold flips upon rotation of the sample by 90°. This indicates that the relative threshold is strongly related to the physical characteristics of the array rather than the preferential alignment of the setup. However, when both polarizations lase, the lasing wavelengths remain within experimental error. A check of the lasing spectra and BFP images (Figure S17 and S18) confirms that the emission pattern is effectively the same for both polarizations, except rotated by 90 deg in k-space. Therefore, the two lasing polarizations

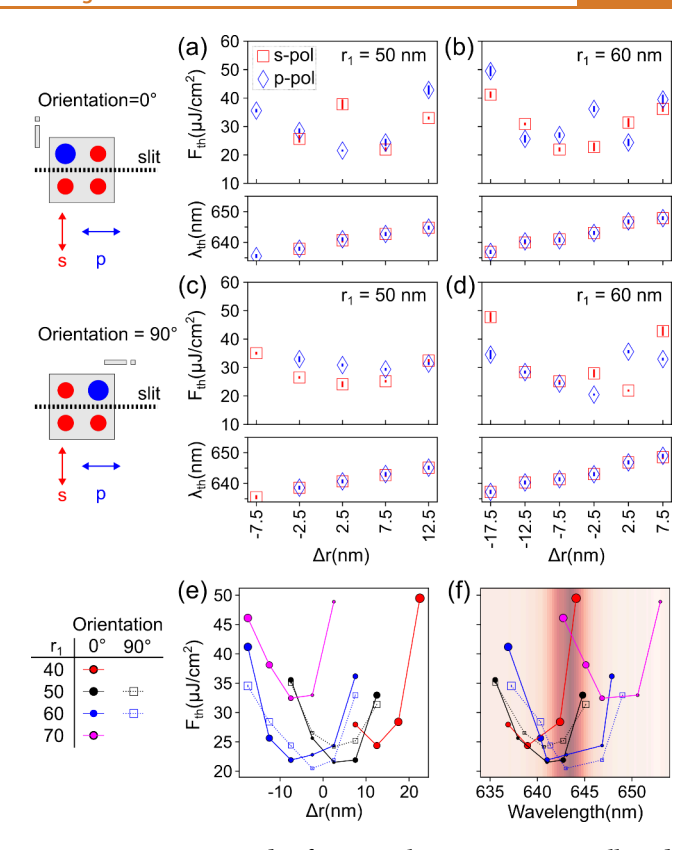


Figure 4. Systematic study of BZF-GR lasing properties. Collected results of lasing thresholds across various arrays and measurement orientations. Variation of s- and p-polarizations lasing thresholds for 0° and 90° rotations for $r_1 = 50$ (a, c) and 60 nm (b, d). Schematics of the array rotation along with the polarizer alignment is shown to the left of the figures. Aggregated data for $r_1 = 40$, 50, 60, and 70 nm and varying Δr . The lowest lasing threshold for each array is plotted against the (e) Δr and (f) lasing wavelength. The ASE spectrum is superimposed in the background of (f).

are determined to originate from the two orthogonally polarized and aligned branches of the TE GRs (TE_1^y, TE_2^x) .

As the QD emitter does not have an intrinsic preferred emission direction, and we are able to observe distinct thresholds of otherwise identical modes, we still expect mode competition between polarizations, and the first mode to start lasing will suppress lasing of other modes as power is increased. Thus, the lower lasing threshold of each array is used to extract an overall trend (Figure 4e,f), where we also include the measurements of r_1 = 40 and 70 nm. We observe that the minimum overall threshold does indeed coincide with the lowest Δr = 2.5 nm. This is easily understood by the α^{-2} scaling of the Q-factor with the asymmetry parameter. The lowest asymmetry (lowest r) array should have the highest Q-factor, and all else equal, exhibit a lower lasing threshold. However, evidently, not all groups of arrays (e.g., $r_1 = 70$ nm) exhibit a lower threshold as decreased. This is also easily understood in terms of spectral overlap (Figure 4f) with the gain. We see that the minimum threshold occurs when the spectral overlap with the gain is the highest and that the data points already begin to form a minimum threshold envelope centered at the ASE peak. This highlights the importance of controlling both asymmetry and mode-wavelength tuning to achieve low-threshold lasing, especially for emitters with a narrow, concentrated gain bandwidth.

An interesting, outstanding issue is the distinct thresholds between the otherwise identical E_x and E_y polarized branches near k=0. It should be noted that at k=0, the two branches are exactly degenerate. Based on the BZF design, we can expect that the direct coupling of the k_x and k_y propagating TE modes which form the BZF-GR at k=0 is enhanced by approximately 4 times over a single unit cell array (e.g., with only 1 pillar in the supercell, Supporting

Information Section 4), while the coupling between k_x and k_y is expected to be largely unchanged. This may be sufficient to effectively decouple the E_x and E_y modes experimentally. For instance, defects or other nonuniformities may then separately adjust the gain threshold of each branch, leading to disparate thresholds for the otherwise degenerate modes. This effect may also be linked to the degree of spatial localization of the lasing emission evident from the optical images of the lasing arrays (Figure S19) and is a matter for further study.

CONCLUSIONS

Overall, we have demonstrated low-threshold vertical emission lasing using BZF-GR modes. Systematic studies of the lasing behavior as a function of asymmetry factor Δr and mode-gain overlap confirm that the lasing threshold can be controlled by adjusting the array asymmetry Δr and tuning the mode-wavelength position relative to the gain spectrum. We expect that if there is sufficient control of the perturbation Δr , the Q-factor of the BZF-GRs can be finely balanced against finite coupling and radiation into the vertical k=0 direction. In this experiment, Δr is limited to a nominal $\Delta r=2.5$ nm based on the fabrication resolution. It should be noted that the realistic Q-factor is determined by the finite extent of the array and intrinsic loss (scattering, parasitic absorption, etc.), which may explain why the lasing threshold is relatively insensitive between $\Delta r=2.5$ and 7.5 nm.

In this design, we also have two nominally identical, but orthogonally polarized, BZF-GR modes lasing at different thresholds. With better control or dynamic tuning of the array, this may enable single-mode, switchable polarization lasing. From a general design perspective, a better understanding of the system is still required to maximize performance. For instance, given the large number of methods available to generate a BZ folding perturbation, evaluating the effect of specific perturbations on the effective quality factor and gain threshold(s) of the target modes will enable a more targeted design. Mode competition and escape channels will eventually need to be carefully considered to control the useful outcoupling of lasing emission from the GR, versus the lasing threshold.

A point to note is that for a small, recognizable perturbation, such as in this case, where the radius of $^1/_4$ of the pillars is perturbed, BZF is a convenient handle to explain the phenomenon observed. It is likely that more optimized designs will eventually require more complex considerations, for instance, how to ensure the s- and p-polarized branches are (de)coupled during lasing, and result in a more complicated perturbation scheme. Other approaches to design multielement unit cells, e.g., the Fourier coupling framework of Noda et al., may provide alternative insights and perspectives on the overall design and optimization methods to explain or construct such BZF structures. With careful design, this BZF system may provide an alternative approach to achieving low-threshold vertical emission lasers suitable for integration with sensitive gain materials such as colloidal QDs.

METHODS

Optical Characterization of BZF Laser. Optical characterization is performed on a customized inverted microscope (Nikon Ti–U). A schematic of the setup is provided in the Supporting Information, Figure S1. For reflectance and transmission measurements, a diffuse halogen lamp is used as the excitation source. For PL and lasing measurements, a 532 nm ns-pulsed laser (Crylas FDS532, \sim 1 ns pulse width, 1 kHz, spot size 9.2×10^{-5} cm² on the sample) is used.

Nanofabrication of TiO₂ Metasurfaces. The basic structure is TiO₂ pillars made by reactive ion etching with a Cr hardmask. Quartz substrates are prepared (JGS2, latech) by cleaning with sonication in acetone and IPA, before the O2 plasma treatment.150 nm TiO2 (Oxford Optofab3000) and 30 nm Cr (Angstrom Evovac) are deposited onto the substrate. A surface treatment of Surpass 3000 (Dishcem) is spin-coated at 4000 rpm for 45 s, followed by DI water at 4000 rpm for 45 s. The substrate is baked at 180 °C for 2 min to dehydrate it. 6 wt % HSQ in MIBK (EM-resist or Dischem) is spincoated at 4000 rpm for 45 s, then annealed at 120 $^{\circ}$ C (2 min)/180 $^{\circ}$ C (2 min). Electron beam lithography is performed by an Elionix ELS-7000 at 100 kV acceleration voltage, 500 pA beam current. The dosage is adjusted for the arrays to remain within the expected size tolerance. The HSQ pattern is developed in a salty developer (4 wt % NaOH, 1 wt % NaCl, Aqueous) for 4 min before rinsing thoroughly with DI water. The HSQ pattern is transferred to the Cr hardmask by reactive ion etching (Oxford OIPT Plasmalab), and the TiO2 pillars are then etched through the hardmask by reactive ion etching (SPTS APS or Oxford Plasmalab 100 Cobra). The hardmask is removed by wet etching in Cr-etchant (Sigma-Aldrich). After sample qualification, an identical cleaning procedure to the first step is performed. Concentrated HSQ, FOX-22 (Dow-corning), is spin-coated at 1000 rpm for 60 s. Annealing is then performed at 300 °C for ~1 h with a ramp-up rate from <150 to 450 $^{\circ}$ C/h. The sample is allowed to cool to room temperature on the hot plate. The FOX-22 is then etched to approximately the same height as the TiO2 pillars. Other various tools are used to calibrate the process, such as SEM (Hitachi SU8 2200), reflectance (Filmetrics), surface profiler (KLA Tencor), and variable angle spectroscopic ellipsometry (J A Woolam).

Synthesis of Compact Continuously Graded QDs (ccg-QDs). *Materials*. Cadmium acetate dihydrate (Cd(OAc)₂·2H₂O, >98%), cadmium oxide (CdO, 99.9%), zinc acetate dihydrate (Zn(OAc)₂·2H₂O, 99.99%, trace metal basis), selenium (Se, 99.99%, trace metals basis), sulfur (S, 99,998%, trace metals basis), trioctylphosphine (TOP, 97%), myristic acid (MA, 98%), oleic acid (OA, 90%), and 1-octadecene (ODE, technical-grade), were purchased from Sigma-Aldrich. Toluene, chloroform, and ethanol were purchased from Merck and used without further purification.

Precursor Preparation. Preparation of Se-TOP (2 M) Precursor. Two M Se-TOP solution was prepared and stored inside the glovebox by fully dissolving the 789.6 mg (10 mmol) of selenium in 5 mL of TOP. Preparation of S-TOP (2 M) precursor: 2 M S-TOP solution was prepared and stored inside the glovebox by fully dissolving 320 mg (10 mmol) of selenium in 5 mL of TOP. Preparation of Cd-oleate $(Cd(OA)_2)$ (0.5 M) precursor: In a 50 mL three-neck round-bottom flask, 2.67 g (10 mmol) of Cd(OAc)₂·2H₂O was dissolved in 10 mL of OA and 10 mL of ODE by degassing at 120 °C under vacuum for 1 h. The final mixture is finally transferred to a sealed bottle and stored in a glovebox for further use. Preparation of Zn-oleate (Zn(OA)₂) (0.5 M) precursor: The Zn-oleate solution was freshly prepared before the synthesis. In a 50 mL three-neck flask, 1.83 g (10 mmol) of Zn(OAc)₂·2H₂O was dissolved in 10 mL of OA, and 10 mL of ODE by degassing at 130 °C under vacuum for 1 h and then kept at 120 °C under nitrogen gas for further use. Shell growth solutions: The synthesis of CdSe/Cd_xZn_{1-x}Se/ZnSe_{0.5}/ZnS (ccg-QDs) was made using the four precursor solutions (A, B, C, and D), which were prepared inside the glovebox. Solution A was prepared by mixing 0.5 mL of Cd(OA₂ (0.5 M)), 0.125 mL of Se-TOP (2 M), and 0.375 mL of the ODE. Solution B was prepared by mixing 1.25 mL of Cd(OA₂ (0.5 M)), 1.25 mL of Se-TOP (2 M), and 2.5 mL of the ODE. Solution C was prepared by mixing 0.5 mL of Se-TOP (2 M) and 0.5 mL of S-TOP (2 M) in 1 mL of the ODE. Solution D was prepared by mixing 0.5 mL of S-TOP (2 M) in 0.5 mL of the ODE.

Synthesis of the QDs. In a typical synthesis, 12.8 mg of CdO (0.1 mmol), 69 mg of myristic acid (0.3 mmol), 0.1 mL of OA (0.3 mmol), and 6 mL of ODE are loaded in a 100 mL three-neck round flask and degassed at 120 °C for 30 min before switching to a nitrogen atmosphere. At 310 °C, 0.1 mL of Se-TOP (2 M) is swiftly injected into the reaction mixture. After 30 s, 1 mL of TOP is added dropwise. After 2 min, 1 mL of Solution A was added continuously into the

reaction flask at a rate of 5 mL/h for 12 min. The solution is then annealed for another 1 min 30 s. For the first coating of graded $Cd_{x}Zn_{1-x}Se$ shell, 2 mL of $Zn(OA)_{2}$ (0.5 M) is swiftly injected into the reaction flask at 300 °C, followed by the dropwise injection of 5 mL of solution B at a rate of 5 mL/h for 60 min. During this injection, 2, 4, and 2 mL of the $Zn(OA)_2$ (0.5 M) mixture were swiftly added at 12, 35.5, and 49.5 min marks, respectively. For the second coating of the ZnSe_{0.5}S_{0.5} shell, 1.5 mL of solution C was continuously introduced into the reaction mixture at 300 °C with a rate of 2 mL/h for 45 min. During this injection, 1 mL of the Zn(OA)₂ (0.5 M) mixture was swiftly added at 15, 30, and 45 min. For the last coating of the ZnS shell, 0.25 mL of solution D was continuously injected into the reaction flask at 300 °C with a rate of 1 mL/h for 15 min. During this injection, 1 mL of the Zn(OA)₂ (0.5 M) mixture was swiftly added at 7 min. The mixture was then cooled down to room temperature, and 18 mL of chloroform was added at 70 °C. To purify the as-synthesized ccg-QDs, ethanol was added to precipitate the QDs, and the mixture was centrifuged at 7000 rpm for 5 min. After centrifugation, the supernatant was discarded, and the precipitate was redispersed in 10 mL of toluene and stored in a glovebox for further

Characterization of ccg-QDs. *TEM.* For ccg-QD imaging, several drops of diluted ccg-QD solution were drop-cast on top of a copper grid covered with an amorphous carbon film. Image acquisition was conducted by using a JEOL TEM 2200F transmission electron microscope operated at 200 kV.

AFM. QD film thickness and roughness were measured with AFM using the scan-assist mode by a Bruker Dimension Icon scanning probe microscope (Bruker 18 Co., Germany). The results are provided in the Supporting Information, Figure S2.

Optical Characterization. Absorbance measurements of the ccg-QDs were recorded using Shimadzu UV and PL spectrophotometers by using a diluted solution of colloidal ccg-QDs. The PL-QY measurement setup was equipped with an Ocean Optics S4000 spectrometer, and an integrating sphere was used. Colloidal ccg-QDs were excited at a wavelength of 405 nm (Cobolt Laser). For femtosecond-pumped ASE measurements, a 400 nm pump laser was obtained by frequency doubling a femtosecond Ti:sapphire 800 nm source (Coherent Astrella F) using an OPA (Coherent Topas Prime). Then, the emission was collected using a fiber-coupled ANDOR spectrometer (monochromator: ANDOR Shamrock 303i, CCD: ANDOR iDus 401). The emission spectra were collected perpendicular to the laser pump. For nanosecond pump ASE measurements, the laser source is a 532 nm ns-pulsed laser (Crylas FDS532, ~1 ns pulse width, 1 kHz). The laser is focused onto the sample through a cylindrical lens into a stripe of width 0.1 mm X length 1 mm. Emission spectra are collected from the edge of the sample with a fiber-coupled spectrometer (Ocean Optics HR4000). One fixed and one movable sharp edge is used to control the length of the stripe. The VSL data is fit to a small signal gain model $I_{\rm PL}(z) = A + \frac{B}{g} [\exp(gz) - 1]$, where g is the modal gain, A is the constant PL offset, and B is the collection efficiency. 46,54,55

ccg-QD Film deposition. A 200 μ L portion of the QD stock solution is precipitated by centrifugation (6000 rpm for 2 min) using a 1:1 EtOH ratio. The precipitates were redispersed in 100 μ L of toluene. Any remaining aggregates were crashed out by centrifugation (8000 rpm for 1 min). The patterned substrates are cleaned using O₂ plasma (100 W for 10 min). Patterned substrates and QD solution are transferred to a nitrogen-filled glovebox, and 60 μ L of the solution is spin-coated on top of the pattern (2000 rpm, 1 min). The resulting film is encapsulated using a carved quartz cap and sealed using epoxy glue. The results are provided in the Supporting Information, Figure

Numerical Simulations. The band structures, Q-factor, and far-field polarization maps were simulated using the finite element method (COMSOL Multiphysics version 6.2). Details of the model parameters and generation of far-field polarization maps are discussed in detail in the Supporting Information, Section 3.

ASSOCIATED CONTENT

Supporting Information

The Supporting Information is available free of charge at https://pubs.acs.org/doi/10.1021/acsnano.5c08419.

Optical characterization of BZF laser; gain material characterization; simulation methods; note on estimated enhancement of 1D coupling coefficient; additional simulations and optical measurements (PDF)

AUTHOR INFORMATION

Corresponding Authors

Lu Ding — Agency for Science, Technology and Research (A*STAR), Institute of Materials Research and Engineering (IMRE), Singapore 138634, Republic of Singapore; orcid.org/0000-0001-8087-2738; Email: dingl@imre.astar.edu.sg

Hilmi Volkan Demir – LUMINOUS! Center of Excellence for Semiconductor Lighting and Displays, The Photonics Institute, School of Electrical and Electronic Engineering, School of Physical and Mathematical Sciences, School of Materials Science and Engineering Nanyang Technological University, Singapore 639798, Singapore; UNAM-Institute of Materials Science and Nanotechnology, The National Nanotechnology Research Center, Department of Electrical and Electronics Engineering, Department of Physics, Bilkent University, Ankara 06800, Turkey; orcid.org/0000-0003-1793-112X; Email: HVDEMIR@ntu.edu.sg

Arseniy I. Kuznetsov — Agency for Science, Technology and Research (A*STAR), Institute of Materials Research and Engineering (IMRE), Singapore 138634, Republic of Singapore; orcid.org/0000-0002-7622-8939; Email: Arseniy_Kuznetsov@imre.a-star.edu.sg

Authors

Matthew R. Chua – Agency for Science, Technology and Research (A*STAR), Institute of Materials Research and Engineering (IMRE), Singapore 138634, Republic of Singapore

Xiao Liang – LUMINOUS! Center of Excellence for Semiconductor Lighting and Displays, The Photonics Institute, School of Electrical and Electronic Engineering, School of Physical and Mathematical Sciences, School of Materials Science and Engineering Nanyang Technological University, Singapore 639798, Singapore

Corentin Dabard – LUMINOUS! Center of Excellence for Semiconductor Lighting and Displays, The Photonics Institute, School of Electrical and Electronic Engineering, School of Physical and Mathematical Sciences, School of Materials Science and Engineering Nanyang Technological University, Singapore 639798, Singapore

Wudeng Wang – Information Science and Engineering College, Dalian Polytechnic University, Dalian 116034, China

Syed Akhil – LUMINOUS! Center of Excellence for Semiconductor Lighting and Displays, The Photonics Institute, School of Electrical and Electronic Engineering, School of Physical and Mathematical Sciences, School of Materials Science and Engineering Nanyang Technological University, Singapore 639798, Singapore

Emek Goksu Durmusoglu – LUMINOUS! Center of Excellence for Semiconductor Lighting and Displays, The Photonics Institute, School of Electrical and Electronic Engineering, School of Physical and Mathematical Sciences, School of Materials Science and Engineering Nanyang Technological University, Singapore 639798, Singapore; orcid.org/0000-0001-6840-8342

Febiana Tjiptoharsono — Agency for Science, Technology and Research (A*STAR), Institute of Materials Research and Engineering (IMRE), Singapore 138634, Republic of Singapore

Ramón Paniagua-Domínguez — Agency for Science, Technology and Research (A*STAR), Institute of Materials Research and Engineering (IMRE), Singapore 138634, Republic of Singapore; orcid.org/0000-0001-7836-681X

Complete contact information is available at: https://pubs.acs.org/10.1021/acsnano.5c08419

Author Contributions

M.R.C. and L.D. conceived the idea, optical characterization, and data analysis; W.W., L.D., and M.R.C. conducted numerical simulation; M.R.C., L.D., and F.T. conducted nanofabrication; X.L. did material synthesis and growth and film encapsulation study; X.L. and C.D. did thin film preparation and encapsulation; S.A. and E.G.D. conducted material and film characterization; M.C. drafted the initial manuscript with input from C.D. regarding the material part; L.D., M.R.C., and R.P.D. participated in discussion; M.C., L.D., H.V.D., and A.I.K. revised and finalized manuscript with inputs from all authors; L.D., H.V.D., and A.I.K. supervised the whole project.

Notes

The authors declare no competing financial interest.

ACKNOWLEDGMENTS

The authors gratefully acknowledge financial support from the National Research Foundation, Singapore, under its NRF Investigatorship programme (NRF-NRFI10-2024-0003) and Singapore Agency for Science, Technology and Research (A*STAR) MTC program under grant number M21J9b0085. The authors would like to thank E. Lassalle and H. K. S. Alnaeemah for valuable discussions. H.V.D. also acknowledges support from TUBITAK 2247-A National Leader Researchers Program (121C266) and TUBA-Turkish Academy of Sciences.

REFERENCES

- (1) Adachi, M. M.; Fan, F.; Sellan, D. P.; Hoogland, S.; Voznyy, O.; Houtepen, A. J.; Parrish, K. D.; Kanjanaboos, P.; Malen, J. A.; Sargent, E. H. Microsecond-Sustained Lasing from Colloidal Quantum Dot Solids. *Nat. Commun.* **2015**, *6*, 8694.
- (2) Fan, F.; Voznyy, O.; Sabatini, R. P.; Bicanic, K. T.; Adachi, M. M.; McBride, J. R.; Reid, K. R.; Park, Y.-S.; Li, X.; Jain, A.; et al. Continuous-Wave Lasing in Colloidal Quantum Dot Solids Enabled by Facet-Selective Epitaxy. *Nature* **2017**, *544*, 75–79.
- (3) Qin, C.; Sandanayaka, A. S. D.; Zhao, C.; Matsushima, T.; Zhang, D.; Fujihara, T.; Adachi, C. Stable Room-Temperature Continuous-Wave Lasing in Quasi-2D Perovskite Films. *Nature* **2020**, 585, 53–57.
- (4) Nasu, R.; Tang, X.; Watanabe, S.; Senevirathne, C. A. M.; Tumen-Ulzii, G.; Matsushima, T.; Adachi, C. Exciton Dynamics and Optically Pumped Lasing in 1-Naphthylmethylamine-Based Quasi-2D Perovskite Films. *Adv. Funct. Mater.* **2023**, *33*, 2301794.
- (5) Roh, K.; Zhao, L.; Rand, B. P. Tuning Laser Threshold within the Large Optical Gain Bandwidth of Halide Perovskite Thin Films. *ACS Photonics* **2021**, *8*, 2548–2554.
- (6) Xing, D.; Chen, M.; Wang, Z.; Deng, C.; Ho, Y.; Lin, B.; Lin, C.; Chen, C.; Delaunay, J. Solution-Processed Perovskite Quantum Dot

- Quasi-BIC Laser from Miniaturized Low-Lateral-Loss Cavity. Adv. Funct. Mater. 2024, 34, 2314953.
- (7) Wu, M.; Ha, S. T.; Shendre, S.; Durmusoglu, E. G.; Koh, W.-K.; Abujetas, D. R.; Sánchez-Gil, J. A.; Paniagua-Domínguez, R.; Demir, H. V.; Kuznetsov, A. I. Room-Temperature Lasing in Colloidal Nanoplatelets via Mie-Resonant Bound States in the Continuum. *Nano Lett.* **2020**, *20*, 6005–6011.
- (8) Tanghe, I.; Samoli, M.; Wagner, I.; Cayan, S. A.; Khan, A. H.; Chen, K.; Hodgkiss, J.; Moreels, I.; Thourhout, D. V.; Hens, Z.; et al. Optical Gain and Lasing from Bulk Cadmium Sulfide Nanocrystals through Bandgap Renormalization. *Nat. Nanotechnol.* **2023**, *18*, 1423–1429
- (9) Ahn, N.; Livache, C.; Pinchetti, V.; Klimov, V. I. Colloidal Semiconductor Nanocrystal Lasers and Laser Diodes. *Chem. Rev.* **2023**, *123*, 8251–8296.
- (10) Bae, W. K.; Padilha, L. A.; Park, Y.-S.; McDaniel, H.; Robel, I.; Pietryga, J. M.; Klimov, V. I. Controlled Alloying of the Core—Shell Interface in CdSe/CdS Quantum Dots for Suppression of Auger Recombination. *ACS Nano* **2013**, *7*, 3411—3419.
- (11) Park, Y.-S.; Bae, W. K.; Baker, T.; Lim, J.; Klimov, V. I. Effect of Auger Recombination on Lasing in Heterostructured Quantum Dots with Engineered Core/Shell Interfaces. *Nano Lett.* **2015**, *15*, 7319—7328.
- (12) Bisschop, S.; Geiregat, P.; Aubert, T.; Hens, Z. The Impact of Core/Shell Sizes on the Optical Gain Characteristics of CdSe/CdS Quantum Dots. ACS Nano 2018, 12, 9011–9021.
- (13) Ahn, N.; Livache, C.; Pinchetti, V.; Jung, H.; Jin, H.; Hahm, D.; Park, Y.-S.; Klimov, V. I. Electrically Driven Amplified Spontaneous Emission from Colloidal Quantum Dots. *Nature* **2023**, *617*, 79–85.
- (14) Cayan, S. A.; Samoli, M.; Tanghe, I.; Lin, C.-Y.; Respekta, D.; Hodgkiss, J. M.; Chen, K.; Hens, Z.; Geiregat, P. Stimulated Emission and Lasing from Bulk CdSe Nanocrystals. *J. Phys. Chem. Lett.* **2024**, *15*, 9836–9843.
- (15) Harankahage, D.; Cassidy, J.; Beavon, J.; Huang, J.; Brown, N.; Berkinsky, D. B.; Marder, A.; Kayira, B.; Montemurri, M.; Anzenbacher, P.; et al. Quantum Shell in a Shell: Engineering Colloidal Nanocrystals for a High-Intensity Excitation Regime. *J. Am. Chem. Soc.* **2023**, *145*, 13326–13334.
- (16) Geiregat, P.; Van Thourhout, D.; Hens, Z. A Bright Future for Colloidal Quantum Dot Lasers. NPG Asia Mater. 2019, 11, 41.
- (17) Kędziora, M.; Opala, A.; Mastria, R.; De Marco, L.; Król, M.; Łempicka-Mirek, K.; Tyszka, K.; Ekielski, M.; Guziewicz, M.; Bogdanowicz, K.; et al. Predesigned Perovskite Crystal Waveguides for Room-Temperature Exciton—Polariton Condensation and Edge Lasing. *Nat. Mater.* **2024**, 23, 1515—1522.
- (18) Lin, Y.; Hsu, K.; Chen, C.; Chan, Y.; Fan, S.; Chen, Y.; Huang, S.; Lee, S.; Lee, Y. Enhanced Emission in Inorganic Halide Perovskite for Room Temperature Continuous-Wave Lasing. *Small* **2025**, 2502081.
- (19) Gao, X.; Lin, J.; Guo, X.; He, G.; Zou, D.; Ishii, T.; Zhang, D.; Zhao, C.; Zhan, H.; Huang, J. S.; et al. Room-Temperature Continuous-Wave Microcavity Lasers from Solution-Processed Smooth Quasi-2D Perovskite Films with Low Thresholds. *J. Phys. Chem. Lett.* **2023**, *14*, 2493–2500.
- (20) Yakunin, S.; Protesescu, L.; Krieg, F.; Bodnarchuk, M. I.; Nedelcu, G.; Humer, M.; De Luca, G.; Fiebig, M.; Heiss, W.; Kovalenko, M. V. Low-Threshold Amplified Spontaneous Emission and Lasing from Colloidal Nanocrystals of Caesium Lead Halide Perovskites. *Nat. Commun.* **2015**, *6*, 8056.
- (21) Song, J.; Ghosh, S.; Deng, X.; Li, C.; Shang, Q.; Liu, X.; Wang, Y.; Gao, X.; Yang, W.; Wang, X.; Zhao, Q.; Shi, K.; Gao, P.; Xing, G.; Xiong, Q.; Zhang, Q.; et al. Room-Temperature Continuous-Wave Pumped Exciton Polariton Condensation in a Perovskite Microcavity. *Sci. Adv.* 2025, 11, No. eadr1652.
- (22) Zou, C.; Cao, X.; Wang, Z.; Yang, Y.; Lian, Y.; Zhao, B.; Di, D. Continuous-Wave Perovskite Polariton Lasers. *Sci. Adv.* **2025**, *11*, No. eadr8826.
- (23) Athanasiou, M.; Papagiorgis, P.; Manoli, A.; Bernasconi, C.; Bodnarchuk, M. I.; Kovalenko, M. V.; Itskos, G. Efficient Amplified

- Spontaneous Emission from Solution-Processed CsPbBr3 Nanocrystal Microcavities under Continuous Wave Excitation. ACS Photonics 2021, 8, 2120–2129.
- (24) Khurgin, J. B.; Noginov, M. A. How Do the Purcell Factor, the Q-Factor, and the Beta Factor Affect the Laser Threshold? *Laser Photonics Rev.* **2021**, *15*, 2000250.
- (25) Hwang, M. S.; Lee, H. C.; Kim, K. H.; Jeong, K. Y.; Kwon, S. H.; Koshelev, K.; Kivshar, Y.; Park, H. G. Ultralow-Threshold Laser Using Super-Bound States in the Continuum. *Nat. Commun.* **2021**, 12, 4135.
- (26) Xie, W.; Stöferle, T.; Rainó, G.; Aubert, T.; Bisschop, S.; Zhu, Y.; Mahrt, R. F.; Geiregat, P.; Brainis, E.; Hens, Z.; Van Thourhout, D.; et al. On-Chip Integrated Quantum-Dot-Silicon-Nitride Microdisk Lasers. *Adv. Mater.* **2017**, *29*, 1604866.
- (27) Huang, L.; Jin, R.; Zhou, C.; Li, G.; Xu, L.; Overvig, A.; Deng, F.; Chen, X.; Lu, W.; Alù, A.; Miroshnichenko, A. E.; et al. Ultrahigh-Q Guided Mode Resonances in an All-Dielectric Metasurface. *Nat. Commun.* **2023**, *14*, 3433.
- (28) Sun, K.; Wei, H.; Chen, W.; Chen, Y.; Cai, Y.; Qiu, C.-W.; Han, Z. Infinite-Q Guided Modes Radiate in the Continuum. *Phys. Rev. B* **2023**, *107*, No. 115415.
- (29) Hsu, C. W.; Zhen, B.; Stone, A. D.; Joannopoulos, J. D.; Soljačić, M. Bound States in the Continuum. *Nat. Rev. Mater.* **2016**, *1*, 1–13
- (30) Ha, S. T.; Li, Q.; Yang, J. K. W.; Demir, H. V.; Brongersma, M. L.; Kuznetsov, A. I. Optoelectronic Metadevices. *Science* **2024**, 386, No. eadm7442.
- (31) Yang, Y.; Peng, C.; Liang, Y.; Li, Z.; Noda, S. Analytical Perspective for Bound States in the Continuum in Photonic Crystal Slabs. *Phys. Rev. Lett.* **2014**, *113*, No. 037401.
- (32) Jin, J.; Yin, X.; Ni, L.; Soljačić, M.; Zhen, B.; Peng, C. Topologically Enabled Ultrahigh-Q Guided Resonances Robust to out-of-Plane Scattering. *Nature* **2019**, *574*, 501–504.
- (33) Kang, M.; Mao, L.; Zhang, S.; Xiao, M.; Xu, H.; Chan, C. T. Merging Bound States in the Continuum by Harnessing Higher-Order Topological Charges. *Light Sci. Appl.* **2022**, *11*, 228.
- (34) Miyai, E.; Sakai, K.; Okano, T.; Kunishi, W.; Ohnishi, D.; Noda, S. Lasers Producing Tailored Beams. *Nature* **2006**, *441*, 946–946.
- (35) Iwahashi, S.; Kurosaka, Y.; Sakai, K.; Kitamura, K.; Takayama, N.; Noda, S. Higher-Order Vector Beams Produced by Photonic-Crystal Lasers. *Opt. Express* **2011**, *19*, 11963–11968.
- (36) Noda, S.; Inoue, T.; Yoshida, M.; Gelleta, J.; Zoysa, M. D.; Ishizaki, K. High-Power and High-Beam-Quality Photonic-Crystal Surface-Emitting Lasers: A Tutorial. *Adv. Opt. Photonics* **2023**, *15*, 977.
- (37) Xu, T.; Yang, S.; Nair, S. V.; Ruda, H. E. Confined Modes in Finite-Size Photonic Crystals. *Phys. Rev. B* **2005**, 72, No. 045126.
- (38) Liang, Y.; Peng, C.; Sakai, K.; Iwahashi, S.; Noda, S. Three-Dimensional Coupled-Wave Analysis for Square-Lattice Photonic Crystal Surface Emitting Lasers with Transverse-Electric Polarization: Finite-Size Effects. *Opt. Express* **2012**, *20*, 15945.
- (39) Ni, L.; Jin, J.; Peng, C.; Li, Z. Analytical and Statistical Investigation on Structural Fluctuations Induced Radiation in Photonic Crystal Slabs. *Opt. Express* **2017**, 25, 5580–5593.
- (40) Yu, S.; Li, Z.; Chai, R.; Liu, W.; Zhou, W.; Cheng, H.; Chen, S. Merging Bound States in the Continuum in the Geometrical Parameter Space. *Phys. Rev. B* **2024**, *109*, No. 115109.
- (41) Wang, W.; Srivastava, Y. K.; Tan, T. C.; Wang, Z.; Singh, R. Brillouin Zone Folding Driven Bound States in the Continuum. *Nat. Commun.* **2023**, *14*, 2811.
- (42) Overvig, A. C.; Cotrufo, M.; Markowitz, M.; Zhou, Y.; Hao, B.; Stensvad, K.; Schardt, C.; Alù, A. Zone-Folded Quasi-Bound State Metasurfaces with Customized, Symmetry-Protected Energy-Momentum Relations. *ACS Photonics* **2023**, *10*, 1832–1840.
- (43) Overvig, A. C.; Malek, S. C.; Carter, M. J.; Shrestha, S.; Yu, N. Selection Rules for Quasibound States in the Continuum. *Phys. Rev. B* **2020**, *102*, No. 035434.
- (44) Fang, J.; Chen, R.; Sharp, D.; Renzi, E. M.; Manna, A.; Kala, A.; Mann, S. A.; Yao, K.; Munley, C.; Rarick, H.; Tang, A.; Pumulo, S.;

- Zheng, Y.; Menon, V. M.; Alù, A.; Majumdar, A.; et al. Million-Q Free Space Meta-Optical Resonator at near-Visible Wavelengths. *Nat. Commun.* **2024**, *15*, 10341.
- (45) de Gaay Fortman, N.; Pal, D.; Schall, P.; Koenderink, A. F. Accessing Beyond-Light Line Dispersion and High-Q Resonances of Dense Plasmon Lattices by Bandfolding. *ACS Photonics* **2025**, *12*, 1163–1173
- (46) Fan, F.; Voznyy, O.; Sabatini, R. P.; Bicanic, K. T.; Adachi, M. M.; McBride, J. R.; Reid, K. R.; Park, Y.-S.; Li, X.; Jain, A.; et al. Continuous-Wave Lasing in Colloidal Quantum Dot Solids Enabled by Facet-Selective Epitaxy. *Nature* **2017**, *544*, 75–79.
- (47) Wu, M.; Ding, L.; Sabatini, R. P.; Sagar, L. K.; Bappi, G.; Paniagua-Domínguez, R.; Sargent, E. H.; Kuznetsov, A. I. Bound State in the Continuum in Nanoantenna-Coupled Slab Waveguide Enables Low-Threshold Quantum-Dot Lasing. *Nano Lett.* **2021**, *21*, 9754–9760
- (48) Tan, Y.; Huang, Y.; Wu, D.; Wang, Y.; Sun, X. W.; Choi, H. W.; Wang, K. Low-Threshold Surface-Emitting Colloidal Quantum-Dot Circular Bragg Laser Array. *Light Sci. Appl.* **2025**, *14*, 36.
- (49) Lim, J.; Park, Y.-S.; Klimov, V. I. Optical Gain in Colloidal Quantum Dots Achieved with Direct-Current Electrical Pumping. *Nat. Mater.* **2018**, *17*, 42–49.
- (50) Wang, Z.; Liu, X.; Wang, P.; Lu, H.; Meng, B.; Zhang, W.; Wang, L.; Wang, Y.; Tong, C. Continuous-Wave Operation of 1550 Nm Low-Threshold Triple-Lattice Photonic-Crystal Surface-Emitting Lasers. *Light Sci. Appl.* **2024**, *13*, 44.
- (51) Inoue, T.; Yoshida, M.; Zoysa, M. D.; Ishizaki, K.; Noda, S. Design of Photonic-Crystal Surface-Emitting Lasers with Enhanced in-Plane Optical Feedback for High-Speed Operation. *Opt. Express* **2020**, *28*, 5050.
- (52) Hirose, K.; Liang, Y.; Kurosaka, Y.; Watanabe, A.; Sugiyama, T.; Noda, S. Watt-Class High-Power, High-Beam-Quality Photonic-Crystal Lasers. *Nat. Photonics* **2014**, *8*, 406–411.
- (53) Yoshida, M.; Katsuno, S.; Inoue, T.; Gelleta, J.; Izumi, K.; De Zoysa, M.; Ishizaki, K.; Noda, S. High-Brightness Scalable Continuous-Wave Single-Mode Photonic-Crystal Laser. *Nature* **2023**, *618*, 727–732.
- (54) Alvarado-Leaños, A. L.; Cortecchia, D.; Folpini, G.; Srimath Kandada, A. R.; Petrozza, A. Optical Gain of Lead Halide Perovskites Measured via the Variable Stripe Length Method: What We Can Learn and How to Avoid Pitfalls. *Adv. Opt. Mater.* **2021**, *9*, 2001773.
- (55) Negro, L. D.; Bettotti, P.; Cazzanelli, M.; Pacifici, D.; Pavesi, L. Applicability Conditions and Experimental Analysis of the Variable Stripe Length Method for Gain Measurements. *Opt. Commun.* **2004**, 229, 337–348.